

Strain engineering and photocatalytic application of single-layer ReS_2

Yan-Ling Li,^{*,†} Yunguo Li,^{*,‡} and Chunlin Tang[†]

*School of Physics and Electronic Engineering, Jiangsu Normal University, Xuzhou,
People's Republic of China, and Earth Sciences, Faculty of Mathematical and Physical
Sciences, University College London, Gower Street, London WC1E 6BT, UK*

E-mail: ylli@jsnu.edu.cn; yunguo.li@ucl.ac.uk

^{*}To whom correspondence should be addressed

[†]School of Physics and Electronic Engineering, Jiangsu Normal University, Xuzhou, People's Republic of China

[‡]Earth Sciences, Faculty of Mathematical and Physical Sciences, University College London, Gower Street, London WC1E 6BT, UK

Abstract

Low-dimensional materials have shown great performances on photocatalytic water splitting owing to their exotic electronic structures and abundant chemical-active sites. We present a theoretical study on the electronic, dynamical, and photocatalytic properties of single-layer ReS_2 under uniaxial strain and shear strain. The single-layer ReS_2 shows anisotropic response to the applied uniaxial strain. The Re–Re direction (a -axis) is less robust than the direction orthornormal to the Re–Re direction (b -axis). The structure is stable in a wide range of b -axial strain with an opened direct band gap, which can effectively improve the photocatalytic efficiency. The ReS_2 structure also shows robustness to the shear strain, and the shear strain is more effective in altering the electronic structure of single-layer ReS_2 . The band gap can be increased up to 1.51 eV with just 1% shear strain. The results suggest that the single-layer ReS_2 can be an efficient photocatalyst for overall water splitting in alkaline water solutions, and the mechanical strain can further improve its catalytic efficiency.

Keywords

Single layer; Photocatalyst; Water splitting; Strain engineering; Shear strain; Dynamic stability

Introduction

The sustainable development of our economy and society hugely depends on the energy that can be supplied in a clean and renewable way. Hydrogen from water splitting driven by solar energy is becoming more and more important and promising, owing to the remarkable advances of materials science and technology in the past decades.^{1,2}

The conversion efficiency from light to chemical energy has been dramatically improved since the discovery of TiO_2 photocatalyst.^{3–6} Qualified photocatalysis have the band gap

over 1.23 eV, and the conduction band (CB) level should be more negative than the H^+/H_2 potential while the (valence band) VB should be more positive than the OH^-/O_2 potential.⁷ Nanostructured materials have shown their advantages in photocatalytic applications.^{5,8,9} Due to the quantum confinement effect, the nanostructured materials exhibit exotic and unique preoperties. Band gap can be opened up, and the increased surface-to-volume ratio can provide more chemical-active sites.^{5,10} These can effectively improve the photocatalytic efficiency. Besides, nanostructured materials coupled with traditional or other nanostructured materials, can further enhance the catalytic properties in the mechanisms of Z-scheme, plasmonic resonance effect and so on.^{11,12} Among the nanostructured materials, two-dimensional (2D) materials is more efficient due to the best surface-to-volume ratio and abundant chemical-active sites. Mostly, in MX_2 ($\text{M}=\text{Mo}, \text{W}, \text{Nb}$; $\text{X}=\text{S}, \text{Se}, \text{Te}$) there is a transition from indirect to direct band gap and improved light absorption when thinning the bulk into single layers.^{13,14}

MX_2 are a series transition metal chalcogenides composed of sandwich X-M-X layers that are stacked by van der Waals forces. The bulk MX_2 often have indirect band gaps.¹⁵ Some of the single layers are semiconductors with the band gap between 1.1 eV and 2.1 eV.¹⁵ They have many promising applications including photocatalytic applications due to the chemical and environmental stability and mechanical flexibility. MoS_2 , MoSe_2 , and WS_2 have shown very high production yield of H_2 .^{5,9,16} Three types of structure have been observed among the MX_2 single layers: 1H- MX_2 (space group $P\bar{6}m2$), 1T- MX_2 (space group $P\bar{3}m1$), and distorted 1T- MX_2 (space group $P-1$). The metal atoms are trigonal prismaticly coordinated in the 1H- MX_2 structure, and octahedrally coordinated in the 1T- MX_2 structure. The distorted 1T- MX_2 is a triclinic structure with distorted X octahedron. It was recently found that the single-layer ReS_2 keeps the distorted 1T- MX_2 structure as in the bulk ReS_2 .¹⁷ It was proved that the ReS_2 layers are electronically and dynamically decoupled in the bulk with very small van der Waals forces. The bulk and single layer possess nearly identical band structure and Raman active modes.^{17,18} This unique character makes

the bulk ReS_2 a pseudo single-layer material. This also creates great advantage for ReS_2 if it can be engineered for photocatalytic applications. The weak coupling between single layers in ReS_2 allows for easy preparation of nanosheets that can provide abundant surfaces and can be easily cocatalyzed with other materials.

However, there is no report on the photocatalytic application of two-dimensional ReS_2 so far. In this paper, we explore the photocatalytic application of the single-layer ReS_2 by using density functional theory (DFT) based calculations. First, we present the electronic and optical properties of the pristine single-layer ReS_2 ; Then we apply engineering uniaxial strain and shear strain to investigate the changes of the electronic and dynamic properties, since strained 2D materials are usually seen in practice; At last, we discuss the photocatalytic potential of the single-layer ReS_2 .

Methodology

The present calculations are based on density functional theory (DFT) and use a plane wave basis set, as implemented in the Vienna Ab initio Simulation Package (VASP).^{19,20} The interaction between the ions and valence electrons is described by the projector augmented wave (PAW) method.^{21–23} Most of the calculations, including structural relaxations and phonon spectra calculations, are done on the level of generalized gradient approximation (GGA), employing the exchange-correlation functional by Perdew, Burke and Ernzerhof (PBE).²⁴ In general, semilocal GGA functionals are known to underestimate the electronic bandgap of semiconductors and insulators, while providing good structural accuracy.^{14,25,26} Considering the effects of half-filled orbitals under varying engineering strain, the $\text{S-}3s^23p^4$ and $\text{Re-}5d^56s^2$ are treated as valence electrons to improve the accuracy of calculations. The convergence criteria is 1×10^{-6} eV/atom for electronic relaxation and 0.01 eV/Å. We performed tests to find suitable cut-off energy and k-mesh. A plane-wave cut-off energy of 500 eV and a k-mesh of $8 \times 8 \times 2$ were enough to reach convergence and used in the calculations.

The phonon dispersions were calculated by means of PHONOPY code,²⁷ which is an implementation of post-process phonon analyzer, from the Hessian matrix calculated using density functional perturbation theory (DFPT) and PBE functional implemented in VASP. We used a $2 \times 2 \times 1$ supercell to calculate the eigenvalues of the Hessian matrix. The phonon-related thermal properties of these compounds were then derived from the calculated phonon spectra.

The bulk ReS_2 corresponds to a triclinic structure, which can be considered as a transformed structure from the hexagonal lattice via Peierls distortion. The single layers in ReS_2 keeps the distorted 1T- MX_2 structure. To facilitate the simulation, we adopted an orthorhombic unitcell for the single layer. Figure 1 shows the structures of the bulk and single-layer ReS_2 .

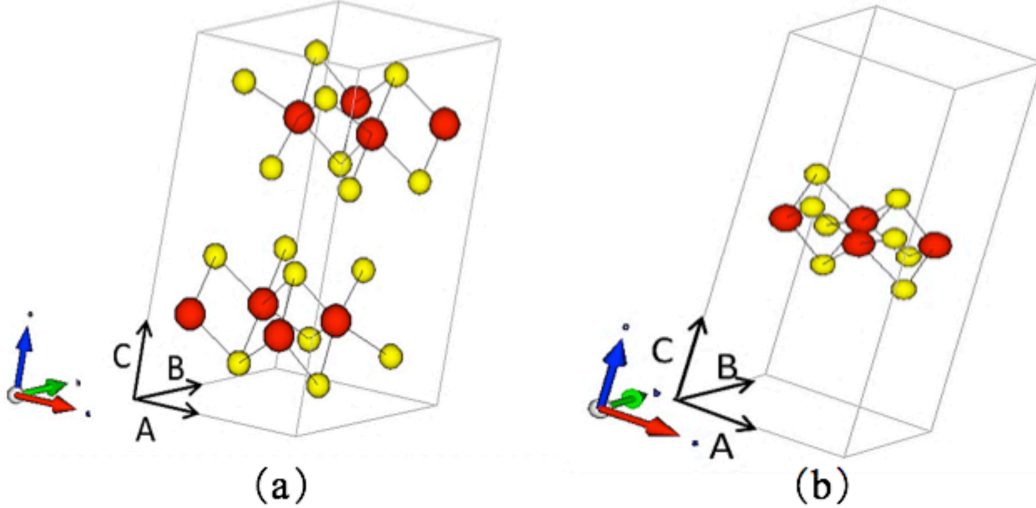


Figure 1: Structures of (a) the bulk and (b) the orthorhombic single-layer ReS_2 . Red and yellow balls indicate Re and S atoms, respectively.

Based on the relaxed ground state, $[-10\%, 10\%]$ uniaxial strain was applied to the a_0 vector in X axis and to the b_0 vector in Y axis, respectively. Then the lattice was relaxed in the in-plane unstrained direction. The shear strain was applied via a shear transformation matrix while maintaining the equilibrium volume.

To better describe the changes of the structure, we labeled the atoms and the angles in

Table 1: Calculated lattice parameters of the single-layer ReS_2 in comparison with experimental data of bulk.

	a(Å)	b(Å)	c(Å)	$\alpha(^{\circ})$	$\beta(^{\circ})$	$\gamma(^{\circ})$	Vol(Å ³)
Bulk ²⁸	6.352	6.446	12.779	91.51	105.17	118.97	434.49
Bulk ²⁹	6.417	6.510	6.461	121.10	88.38	106.47	219.32
Single layer	6.586	5.828	16.657	90	90	90	639.30

the single-layer ReS_2 as depicted in Figure 2.

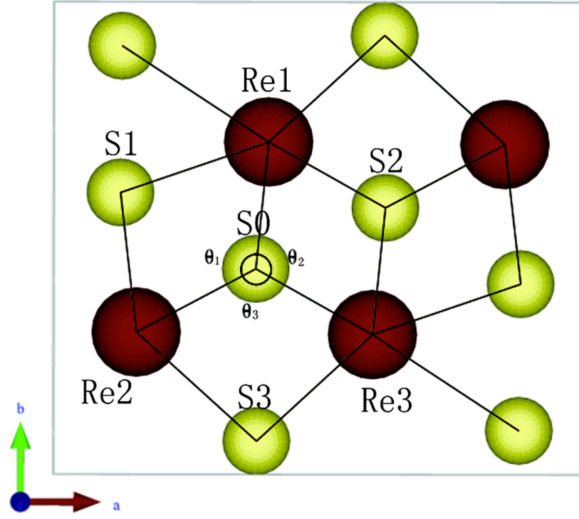


Figure 2: The top view of the single-layer ReS_2 unitcell

Results and Discussion

Ground-state single-layer ReS_2

Table 1 shows the calculated lattice parameters of the single-layer ReS_2 in comparison with bulk. The calculated lateral area of the single-layer ReS_2 is very close to that of bulk. Besides, the calculated Re-S bond length (2.34~2.46Å) matches with that of experimental data and that of LDA (local density approximation) data.¹⁸

Besides, the calculated band gap of the single-layer ReS_2 is 1.39 eV as shown in Figure 3. This value is close to the experimental value (1.55 eV) and other calculated value (1.43 eV).¹⁷ It suggests the good choice of our method. The band gap calculated using HSE06 is 2.00

eV, which is highly overestimated. Such a phenomenon is usually seen in two-dimensional systems.¹⁴ Hybrid functionals usually overestimate the band gap of single layers, while the semi-local functionals can provide closer values to the experimental data. This can be attributed to the weak interlayer van der Waals interactions. Because of that, there is no sharp cutoff of the charge density on the surface and thus can be accurately described by the generalized gradient approximation. We also calculated the band structures of the bulk, four-layer, and two-layer ReS₂. They share much the same band structure. The calculated band gap of the bulk ReS₂ is 1.32 eV, which is also very close to that of the single layer.

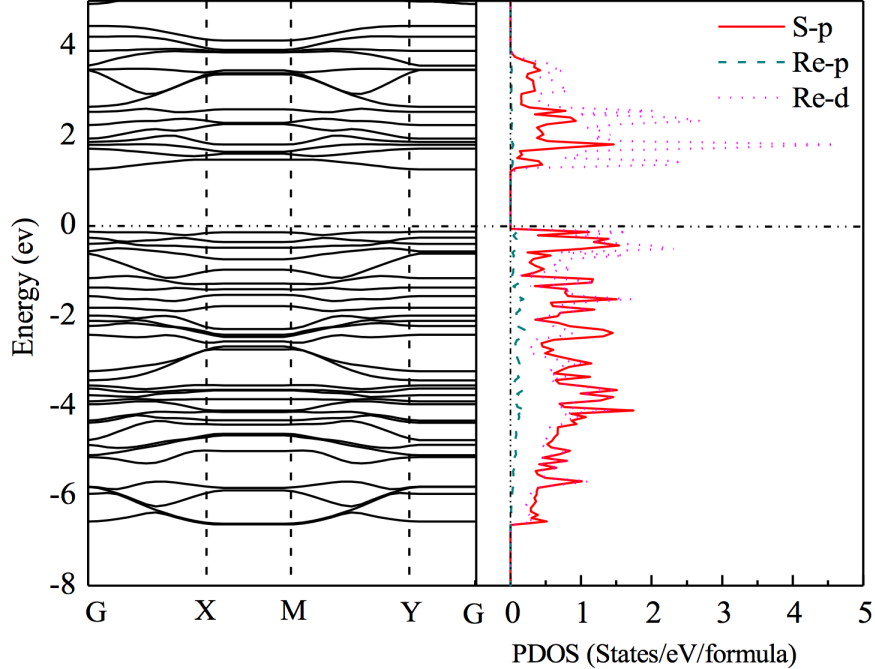


Figure 3: Band structure and PDOS (Patial density of states) of the single-layer ReS₂.

As shown in Figure 3, the single-layer ReS₂ is a direct band gap semiconductor. There is a strong hybridization between the Re-*d* states and S-*p* states. This is similar to other transition metal dichalcogenides. The energy of Re-*d* states is higher than that of S-*p* states, so the upper part of the valence band is dominated by the Re-*d* states. The valence band maximum, or the highest occupied crystal orbital (HOCO) is from the filled antibonding states of $(d_{x^2-y^2}, d_{xy}) + (p_x, p_y)$ hybridization. The conduction band minimum, or the

lowest unoccupied crystal orbital (LUCO) is from the empty antibonding of $d_{z^2} + (p_x, p_y)$ hybridization.

The optical band gaps of the bulk and single-layer ReS_2 are matching with their electrical band gaps, as can be seen in Figure 4. The bulk and single-layer ReS_2 are sharing very similar optical properties as expected. Their imaginary parts of the dynamic dielectric function almost coincide with each other, showing great similarity in light absorption character. Especially, the absorption is more effective for visible light ranging from 1.6 to 3.1 eV.

The single-layer ReS_2 is dynamically stable as there is no imaginary frequency in phonon spectrum shown in Figure 5. There are four formula units of ReS_2 in the single-layer unitcell as seen in Figure 1. Therefore, it has 36 phonon branches which includes three acoustic branches and 33 optical branches. The phonon PDOS (Partial density of states) suggests that the low-frequency region is equally populated by Re and S. The high-frequency region, namely the optical branches is mainly dominated by S. This is attributed to the light weight and low coordination number of S. Besides, there is a gap separating two regions (10.46-11.40 THz and 6.58-7.05 THz) in the high-frequency region. The three acoustic branches are not degenerate, suggesting anisotropic nature of the structure.

Strain and stability

In this section, we try to explore the elastic limit of the single-layer ReS_2 . The lattice and the internal coordinates were fully relaxed after applying uniaxial strain, while only the internal coordinates were relaxed after applying the shear strain.

Figure 6 shows the changes of bond angles under uniaxial strain along a -axis and b -axis. The three curves correspond to the three angles labeled in Figure 2. The varying bond angles exhibit the similar trend for both a -axial and b -axial straining. Overall, the bond angles increase with increasing strain, but the minima appears at -9% compression strain. The angles increase dramatically if the compression continues. This suggests the elastic compression limit of the single-layer ReS_2 . The changes of the bond lengths are similar to

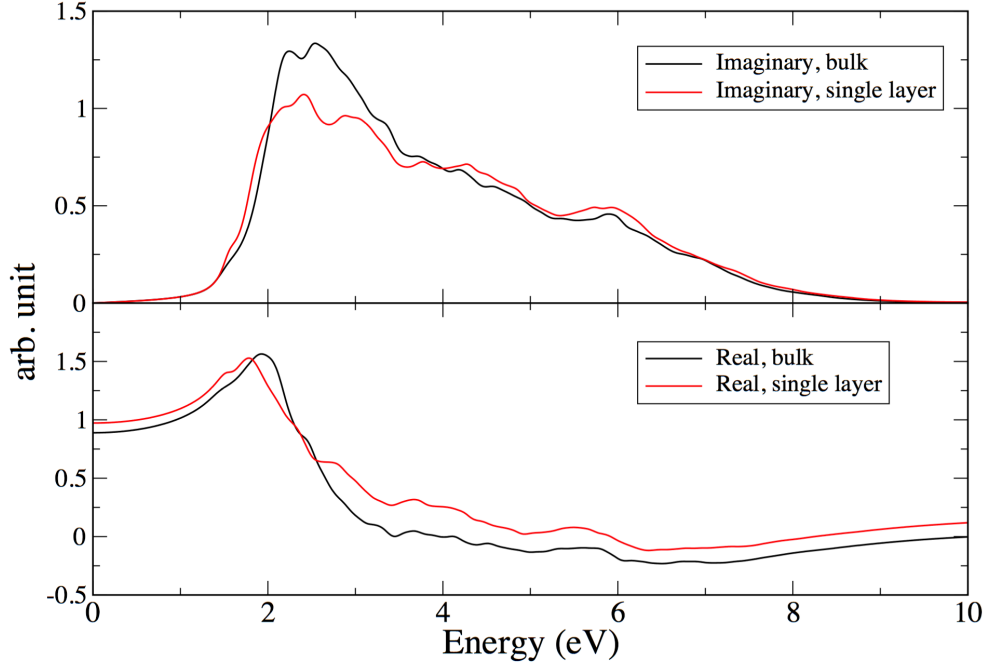


Figure 4: Optical properties of the single-layer ReS_2 . Upper panel and lower panel show the imaginary (Im) part and real part (Re) of the dynamic dielectric function, respectively.

the angles under strain as shown in Figure 7. Worth of notice is that θ_3 shows different responses to a -axial strain and b -axial strain. It increases with increasing a -axial strain, but decreases with increasing b -axial strain. Besides, θ_1 and θ_2 are more sensitive to b -axial strain.

To identify the dynamic stability of the single-layer ReS_2 under strain, we calculated the phonon spectra of the structure under different straining conditions. From the phonon spectra in Figures 8 and 9, we can obtain: First, the structure becomes dynamically unstable when the compression strain exceeds 6% along a -axis and 8% along b -axis. This suggests that b -axis is more resistant to compression; Second, imaginary frequencies emerge when a -axial strain reaches to 10%, but there are no imaginary frequencies when applying 10% b -axial strain. This also suggests the good resistance to tensile strain along b -axis.

We also investigated the dynamic stability of single-layer ReS_2 under shear strain. Figure 10 shows the phonon spectra under different shear strain. It can be seen that there is an immediate change of phonon spectra upon 1% shear straining. The frequencies of the acoustic

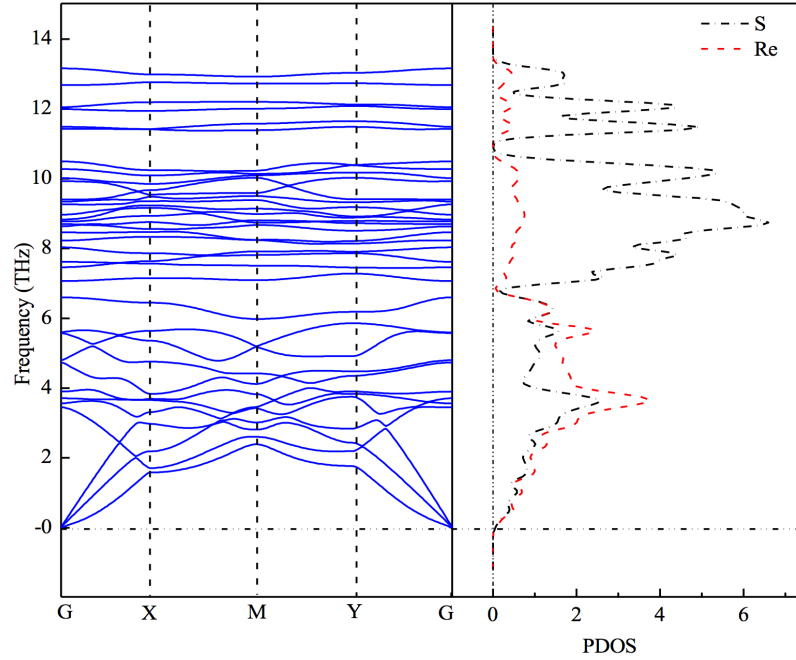


Figure 5: Phonon spectra and phonon PDOS (Patial density of states) of the single-layer ReS_2 .

branches become smaller and softening occurs. Some optical branches between 7 THz to 11 THz start to plunge into the low-frequency region, while the higher optical branches start to climb up. The phonon PDOS shows that Re contributes more to the low-frequency region and S contributes more to the high-frequency region. With increasing shear strain, the phonon branches continue to soften. Imaginary frequency starts to emerge when the shear strain reaches up to 10%. Though such small amount of imaginary frequency can be eliminated by temperature and temperature-induced electron-phonon coupling, it still suggests that the structure start to be dynamically unstable. When the shear strain reaches to 15%, large amount of imaginary frequencies emerge and the structure collapses.

Electronic structure and photocatalytic application

We have shown the elastic limits of the single-layer ReS_2 in last Section. Now we can have a look at the variation of the electronic structure and photocatalytic properties under

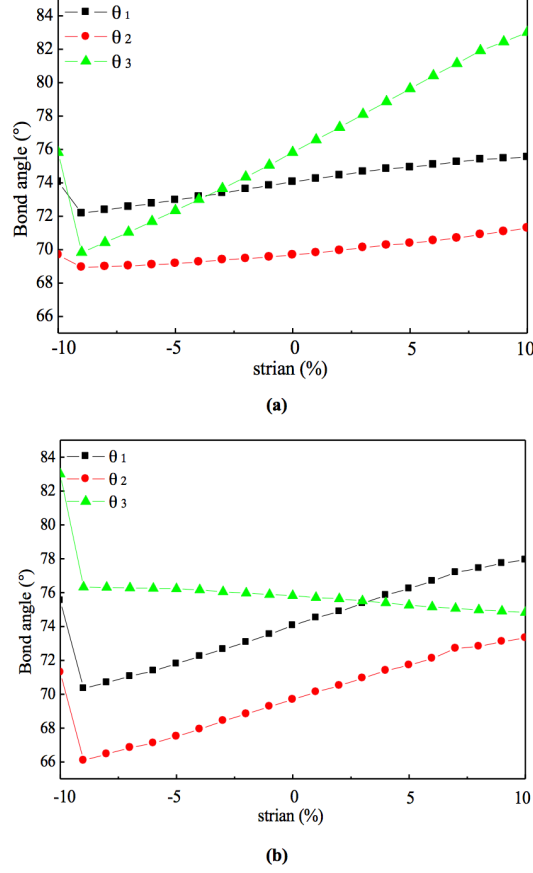


Figure 6: Bond angles as a function of (a) the a -axial strain and (b) the b -axial strain.

engineering strain. It has been reported that the band edge levels of the single-layer MoS_2 are at the very positions for overall water splitting. The CBM and VBM of the single-layer ReS_2 are expected to be higher than those of MoS_2 since the energy of the $5d$ orbital of Re is higher than that of the $4d$ orbital of Mo.

Figure 11 and Figure 12 show the evolution of band gap and band edge levels under engineering uniaxial strain. When applying -10% to 10% uniaxial strain, there is a transition from indirect band gap to direct band gap and then to indirect band gap. Specifically, the single layer keeps to be a direct band gap semiconductor when applying -1%~4% a -axial strain or -6%~1% b -axial strain.

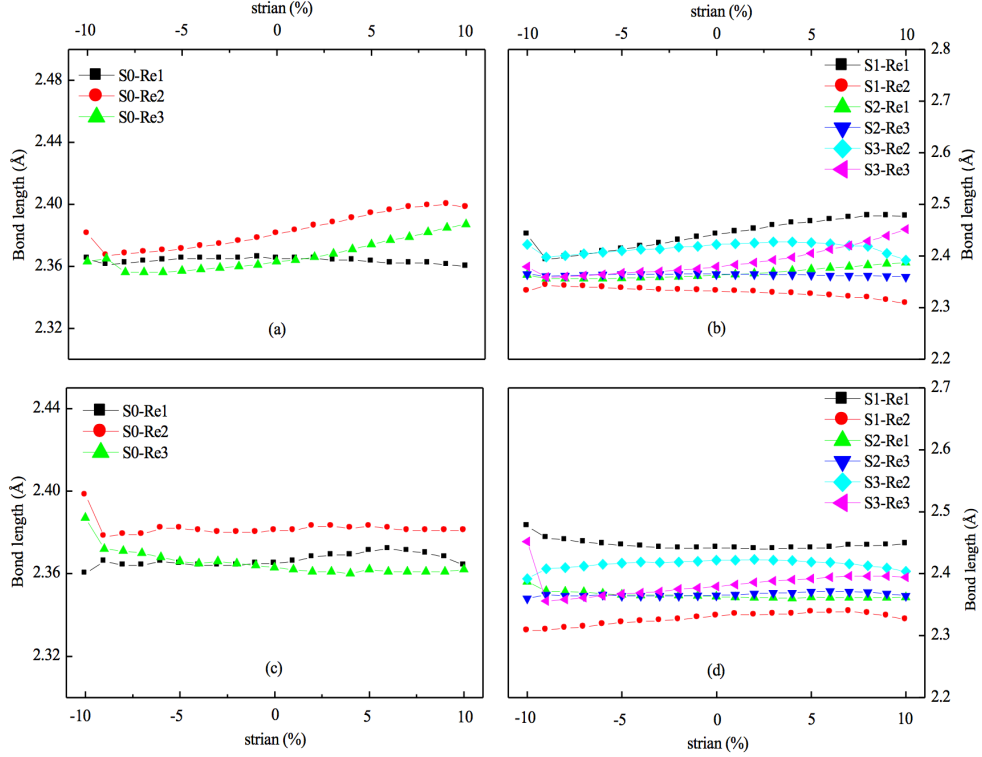


Figure 7: Bond lengths as a function of (a and b) the a -axial strain and (c and d) the b -axial strain.

The energy level of VBM does not show evident variation under straining, while the level of CBM is very more sensitive to straining. In addition, the level of CBM is more sensitive to tensile than to compression. This is because the LUCO (where the CBM is located) is hybridized between d_{z^2} and P_x, P_y , which has more σ bond nature, which strongly depends on the bond length. The compression has little effect on the bond lengths, but the tensile has more evident effects on bond lengths as can be seen in Figure 7. The bond lengths increase rapidly upon tensile straining, which effectively reduces the charge overlap between d_{z^2} and P_x, P_y orbitals and lowers the level of CBM.

As can be seen in Figure 11 and Figure 12, the band gap of single-layer ReS_2 is direct and over 1.23 eV around the equilibrium lattice. However, the band edge alignment with respect to the water redox potentials shows that the single-layer ReS_2 is not suitable for overall water splitting in pure water.

In practical process, the redox reaction not only depends on the band structure of photocatalysis, but also depends on the pH value of the water solution. Specifically,

$$E_{O_2/H_2O}^{OX} = -4.44 + (-1)(+1.229) + pH \times 0.0592eV - \frac{0.0592}{4} \log_{10}(pO_2) \quad (1)$$

$$E_{H^+/H_2}^{OX} = -4.44 + (-1)(+0.401) - pOH \times 0.0592eV - \frac{0.0592}{4} \log_{10}(pO_2) \quad (2)$$

where

$$pOH + pH = 14 \quad (3)$$

pO_2 designates the partial pressure of oxygen in ambient conditions. It is clear that the increase of pH value can shift the redox potential upwards. So, the water redox potentials can be adjusted to suitable level to enable the single-layer Re_2 as overall water-splitting photocatalyst. When the pH value is no less than 12, the water redox potential will be shifted upwards by over 0.7 eV. Then the CBM of the single-layer Re_2 will be higher than the water oxidation potential, and the single-layer Re_2 is able to catalyze overall water splitting.

Figure 13 and Figure 14 describe the variation of electronic structure under shear strain. The band gap is immediately increased to 1.51 eV and becomes to indirect band gap after 1% shear strain. The increase of band gap is due to the upward shift of CBM. The applied shear strain can effectively increase the overlap between d_{z^2} and P_x, P_y orbitals, and thus push up the LUCO. As can be seen from Figure 14, the peak of CBM under varying shear strain is at about the same level as under uniaxial compression strain. This suggests that 1% shear strain help reach to the maximum overlap between d_{z^2} and P_x, P_y orbitals. The VBM does not show visible change under shear strain. So, the shear strain also can not improve the band edge alignment of the single-layer Re_2 . The overall water splitting by the single-layer Re_2 has to be conducted in alkaline water solution.

As described above, the uniaxial strain in a medium range can tune the band gap (and also the light absorption) while keeping direct band gap nature, which can effectively improve

the efficiency of light-to-chemical conversion. The shear strain can only increase the band gap, which may improve the absorption of the high-energy photons. However, the change of the band gap to indirect band gap, may lower the overall efficiency of light-to-chemical conversion.

Conclusions

We have investigated the potential of the single-layer ReS_2 as a photocatalyst based on DFT calculations. It is predicted that the single-layer ReS_2 can be an efficient photocatalyst for overall water splitting in alkaline water solution. The structural anisotropy of the single-layer ReS_2 is reflected by the different responses to the uniaxial strains along a -axis and along b -axis. The b -axial direction is more robust and stretchable than the a -axial direction. The band gap keeps to be direct in a large range of uniaxial strain, and the uniaxial strain can help improve the efficiency of light-to-chemical conversion. The 1% shear strain can immediately push up the CBM level and increase the band gap, but it also induces the indirect band gap. Then the gained improvement on high-energy phonon harvesting may be cancelled out by the lowered overall light absorption efficiency. It is suggested to avoid the shear-straining state when using the single-layer Re_2 as a photocatalyst.

ASSOCIATED CONTENT

Supporting Information.

Crystal structure CIF file. This material is available free of charge via the Internet at <http://pubs.acs.org>.

AUTHOR INFORMATION

Corresponding Author

*Yan-Ling Li, School of Physics and Electronic Engineering, Jiangsu Normal University, Xuzhou, People’s Republic of China. Email: ylli@jsnu.edu.cn

*Yunguo Li, Earth Sciences, Faculty of Mathematical and Physical Sciences, University College London, Gower Street, London WC1E 6BT, UK. Email: yunguo.li@ucl.ac.uk

Notes

The authors declare no competing financial interest.

Funding Sources

Financial support from is gratefully acknowledged.

ACKNOWLEDGEMENT

Y.-L.L. acknowledges support from the NSFC (11347007), Qing Lan Project and the Priority Academic Program Development of Jiangsu Higher Education Institutions (PAPD). We thank Dr. Baisheng Sa for fruitful discussions.

References

- (1) Kubacka, A.; Fernández-García, M.; Colón, G. *Chemical Reviews* **2011**, *112*, 1555–1614.
- (2) Osterloh, F. E. *Chemical Society Reviews* **2013**, *42*, 2294–2320.

- (3) Yu, J.; Xu, C.-Y.; Ma, F.-X.; Hu, S.-P.; Zhang, Y.-W.; Zhen, L. *ACS Applied Materials & Interfaces* **2014**, *6*, 22370–22377, PMID: 25411908.
- (4) De Lasa, H.; Serrano-Rosales, B. *Advances in Chemical Engineering: Photocatalytic Technologies*; Academic Press, 2009; Vol. 36.
- (5) Maitra, U.; Gupta, U.; De, M.; Datta, R.; Govindaraj, A.; Rao, C. N. R. *Angewandte Chemie International Edition* **2013**, *52*, 13057–13061.
- (6) Kudo, A.; Miseki, Y. *Chem. Soc. Rev.* **2009**, *38*, 253–278.
- (7) Lewerenz, H.-J., Peter, L., Eds. *Photoelectrochemical Water Splitting*; RSC Energy and Environment Series; The Royal Society of Chemistry, 2013; pp P001–468.
- (8) Chen, J.; Wu, X.-J.; Yin, L.; Li, B.; Hong, X.; Fan, Z.; Chen, B.; Xue, C.; Zhang, H. *Angewandte Chemie International Edition* **2015**, *54*, 1210–1214.
- (9) Mahler, B.; Hoepfner, V.; Liao, K.; Ozin, G. A. *Journal of the American Chemical Society* **2014**, *136*, 14121–14127, PMID: 25220034.
- (10) Sun, Y.; Gao, S.; Lei, F.; Xie, Y. *Chem. Soc. Rev.* **2015**, *44*, 623–636.
- (11) Kudo, A. *MRS Bulletin* **2011**, *36*, 32–38.
- (12) Awazu, K.; Fujimaki, M.; Rockstuhl, C.; Tominaga, J.; Murakami, H.; Ohki, Y.; Yoshida, N.; Watanabe, T. *Journal of the American Chemical Society* **2008**, *130*, 1676–1680, PMID: 18189392.
- (13) Álvarez, M. P.; del Corro, E.; Morales-García, Á.; Kavan, L.; Kalbac, M.; Frank, O. *Nano Letters* **2015**, *null*, null, PMID: 25915008.
- (14) Li, Y.; Li, Y.-L.; Araujo, C. M.; Luo, W.; Ahuja, R. *Catal. Sci. Technol.* **2013**, *3*, 2214–2220.

- (15) Li, Y.; Li, Y.-L.; Sun, W.; Ahuja, R. *Computational Materials Science* **2014**, *92*, 206 – 212.
- (16) Gupta, U.; Naidu, B. S.; Maitra, U.; Singh, A.; Shirodkar, S. N.; Waghmare, U. V.; Rao, C. N. R. *APL Materials* **2014**, *2*, 092802.
- (17) Tongay, S. et al. *Nat Commun* **2014**, *5*.
- (18) Feng, Y.; Zhou, W.; Wang, Y.; Zhou, J.; Liu, E.; Fu, Y.; Ni, Z.; Wu, X.; Yuan, H.; Miao, F.; Wang, B.; Wan, X.; Xing, D. *Phys. Rev. B* **2015**, *92*, 054110.
- (19) Kresse, G.; Joubert, D. *Phys. Rev. B* **1999**, *59*, 1758.
- (20) Blöchl, P. E. *Phys. Rev. B* **1994**, *50*, 17953.
- (21) Kresse, G.; Furthmüller, J. *Comput. Mater. Sci.* **1996**, *6*, 15–50.
- (22) Kresse, G.; Furthmüller, J. *Phys. Rev. B* **1996**, *54*, 11169.
- (23) Kresse, G.; Hafner, J. *Phys. Rev. B* **1993**, *48*, 13115.
- (24) Perdew, J. P.; Burke, K.; Ernzerhof, M. *Phys. Rev. Lett.* **1996**, *77*, 3865–3868.
- (25) Bilc, D. I.; Orlando, R.; Shaltaf, R.; Rignanese, G.-M.; Íñiguez, J.; Ghosez, P. *Phys. Rev. B* **2008**, *77*, 165107.
- (26) Sa, B.; Li, Y.-L.; Qi, J.; Ahuja, R.; Sun, Z. *The Journal of Physical Chemistry C* **2014**, *118*, 26560–26568.
- (27) Togo, A.; Oba, F.; Tanaka, I. *Phys. Rev. B* **2008**, *78*, 134106.
- (28) Lamfers, H.-J.; Meetsma, A.; Wiegers, G.; De Boer, J. *Journal of alloys and compounds* **1996**, *241*, 34–39.
- (29) Murray, H.; Kelty, S.; Chianelli, R.; Day, C. *Inorganic Chemistry* **1994**, *33*, 4418–4420.

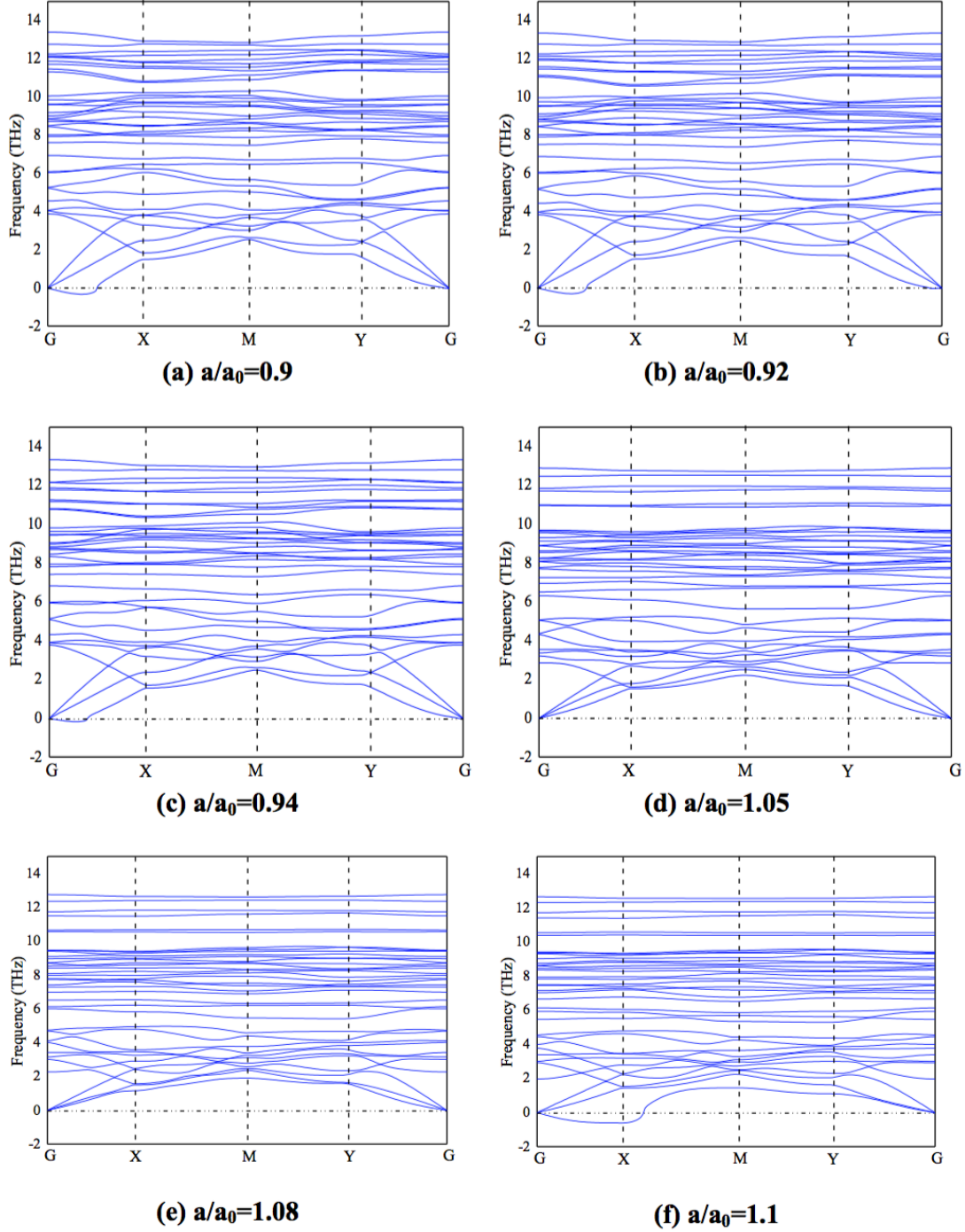
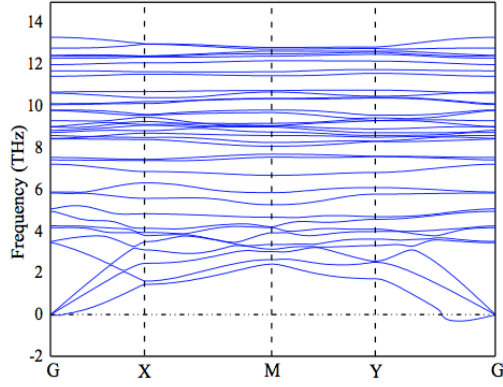
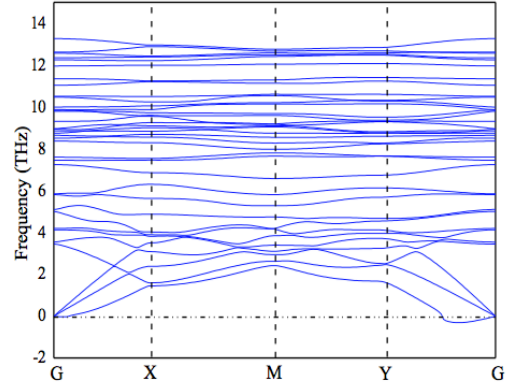


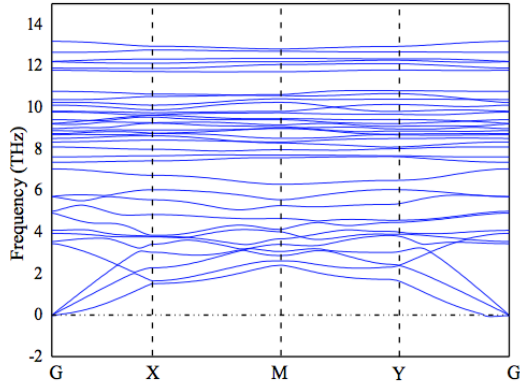
Figure 8: Phonon dispersion curves of single-layer ReS_2 under (a) 10%, (b) 8%, and (c) 6% compression strain and (d) 5%, (e) 8% and (f) 10% tensile strain along the a axis.



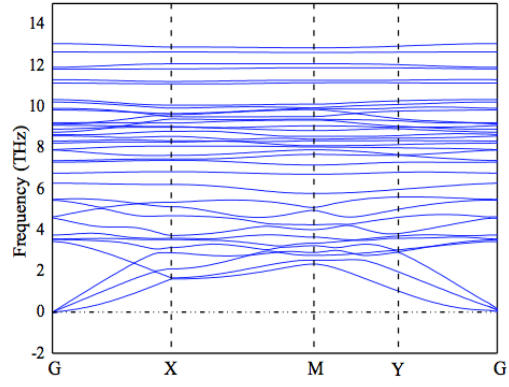
(a) $b/b_0=0.9$



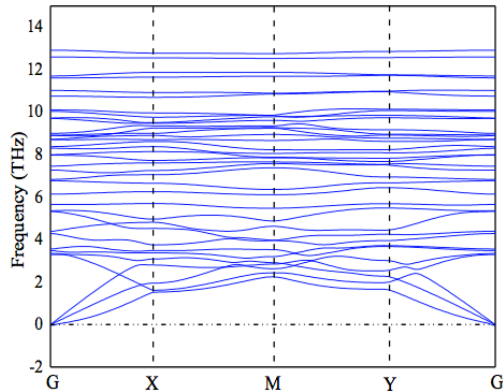
(b) $b/b_0=0.92$



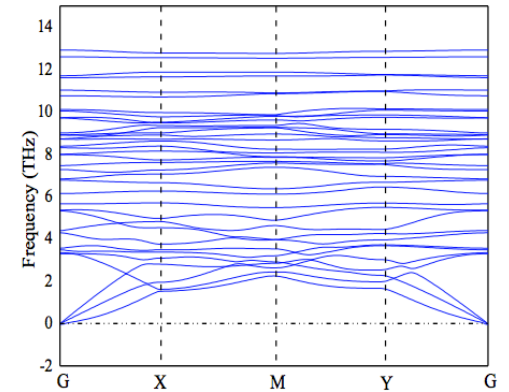
(c) $b/b_0=0.96$



(d) $b/b_0=1.02$



(e) $b/b_0=1.06$



(f) $b/b_0=1.1$

Figure 9: Phonon dispersion curves of single-layer ReS_2 under (a) 10%, (b) 8%, (c) 4% compression strain and (d) 2%, (e) 6%, and (f) 10% tensile strain along the b axis.

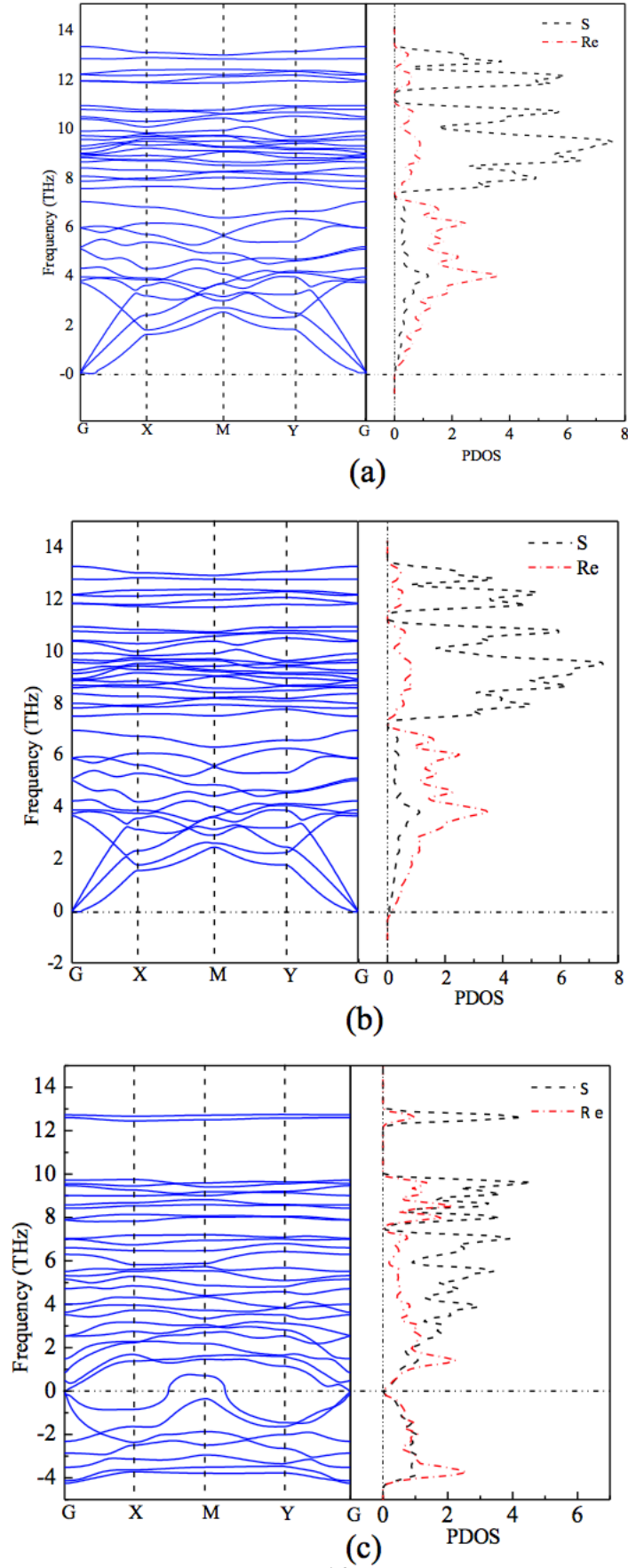


Figure 10: Phonon spectra and PDOS of single-layer ReS_2 under (a) 1%, (b) 10%, (c) 15% shear strain.

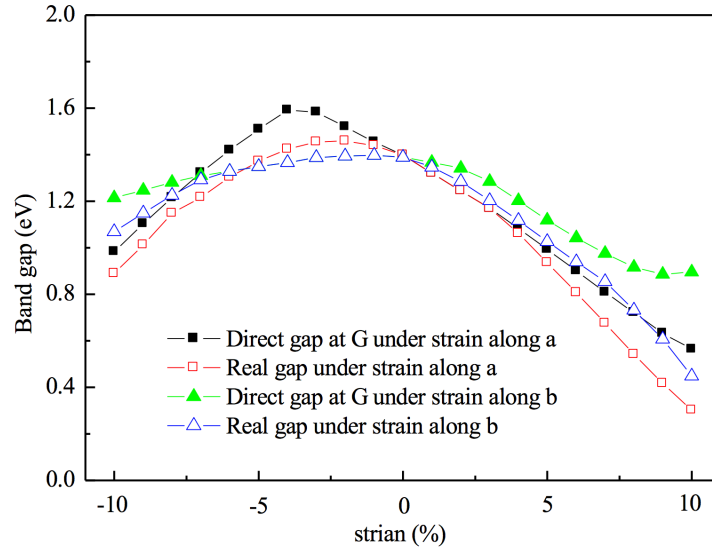


Figure 11: Band gap of single-layer ReS₂ under uniaxial strain.

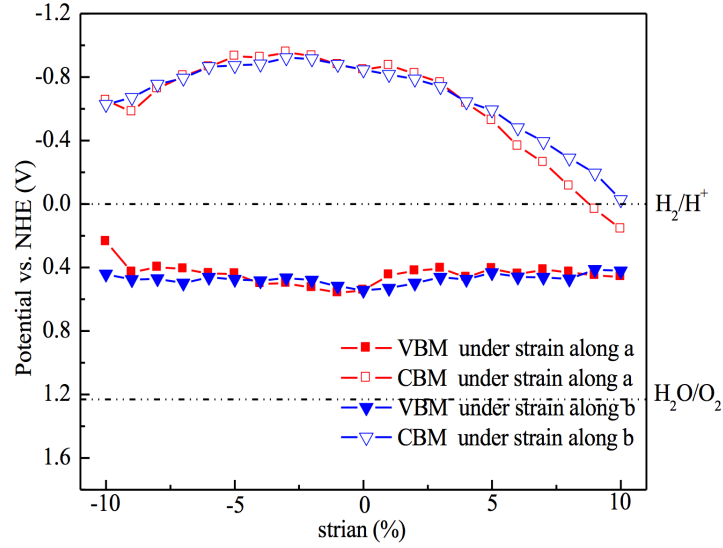


Figure 12: The evolution of the VBM and CBM of single-layer ReS₂ under applied uniaxial strain.

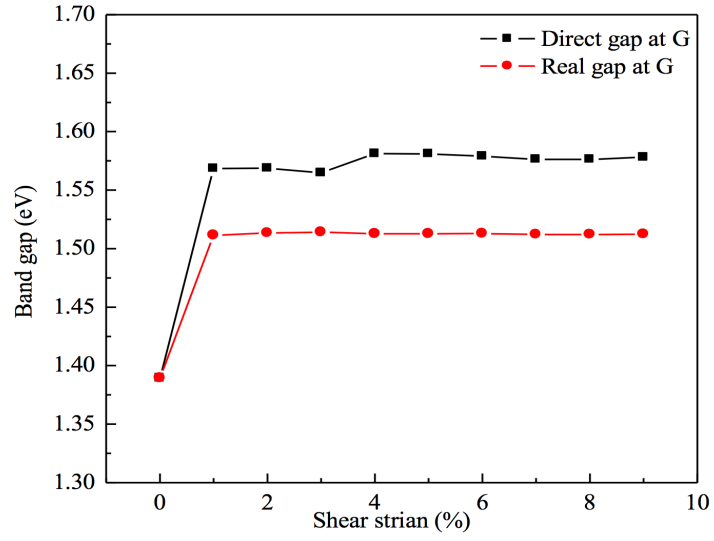


Figure 13: Band gap of single-layer ReS_2 under shear strain.

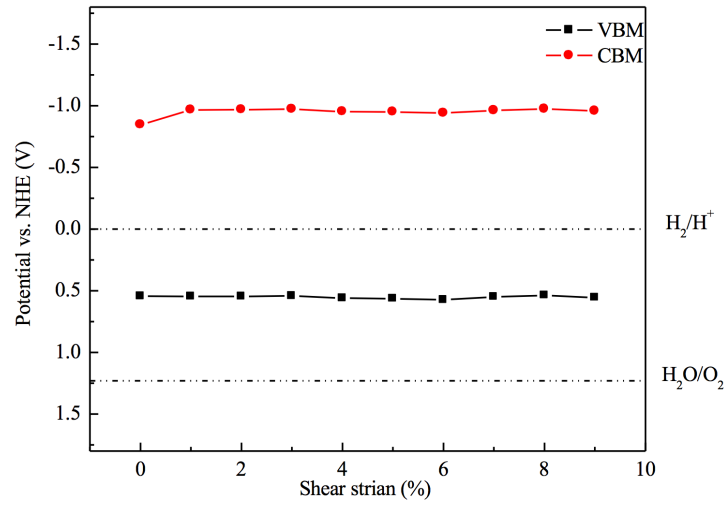


Figure 14: The evolution of the VBM and CBM of single-layer ReS_2 under applied shear strain.